

# Direct Observations of Surface-Wave Eigenfunctions at the Homestake 3D Array

by Patrick Meyers,<sup>\*</sup> Daniel C. Bowden,<sup>†</sup> Tanner Prestegard, Victor C. Tsai,<sup>‡</sup>  
Vuk Mandic, Gary Pavlis, and Ross Caton

**Abstract** Despite the theory for both Rayleigh and Love waves being well accepted and the theoretical predictions accurately matching observations, the direct observation of their quantifiable decay with depth has never been measured in the Earth's crust. In this work, we present observations of the quantifiable decay with depth of surface-wave eigenfunctions. This is done by making direct observations of both Rayleigh-wave and Love-wave eigenfunction amplitudes over a range of depths using data collected at the 3D Homestake array for a suite of nearby mine blasts. Observations of amplitudes over a range of frequencies from 0.4 to 1.2 Hz are consistent with theoretical eigenfunction predictions. They show a clear exponential decay of amplitudes with increasing depth and a reversal in sign of the radial-component Rayleigh-wave eigenfunction at large depths, as predicted for fundamental-mode Rayleigh waves. Minor discrepancies between the observed eigenfunctions and those predicted using estimates of the local velocity structure suggest that the observed eigenfunctions could be used to improve the velocity model. Our results confirm that both Rayleigh and Love waves have the depth dependence that they have long been assumed to have. This is an important direct validation of a classic theoretical result in geophysics and provides new observational evidence that classical seismological surface-wave theory can be used to accurately infer properties of Earth structure and earthquake sources.

## Introduction

The existence of surface waves has been well predicted and described since at least 1885 by Lord Rayleigh (Rayleigh, 1885). Specifically, the interaction of compressional ( $P$ ) and shear ( $S$ ) waves with a free surface will set up Rayleigh waves (from  $P$  and vertically polarized  $S$ ) along that surface, and low near-surface  $S$ -wave velocities will result in Love waves (from horizontally polarized  $S$ ). The surface-wave propagation velocities and amplitudes depend on subsurface properties in a predictable manner. Surface waves have been observed and used in many studies in the Earth sciences, for example, to constrain crustal properties from surface-wave dispersion (e.g., Dziewonski and Anderson, 1981; Shapiro *et al.*, 2005) or ellipticity (e.g., Nakamura, 1989; Lin *et al.*, 2008), to image and understand earthquake source processes (e.g., Duputel *et al.*, 2012), and

to better understand the strength of shaking that may occur in future earthquakes (e.g., Kawase and Aki, 1989).

Because of these applications, the nature of surface-wave propagation is well accepted in the literature. However, one of the defining characteristics of these surface waves, that they decay in amplitude in an exponential manner as a function of depth, has never been directly observed for the Earth's crust. This decay in amplitude is described by the eigenfunctions that result from solving the equations of motion (e.g., Takeuchi and Saito, 1972; Aki and Richards, 2002), and actual particle-motion amplitudes should exactly match these expectations. Unfortunately, most seismic observations are constrained to the Earth's surface, and borehole instruments have generally been too sparsely spaced for the direct observation of surface-wave eigenfunctions to be clearly observed. Although fault-zone-trapped waves, which are somewhat analogous to surface waves, have been observed (e.g., Li and Leary, 1990) and ambient seismic noise is generally observed to decrease with depth (e.g., Peterson, 1993; Mandic *et al.*, 2018), neither of these observations is a direct measurement of surface-wave eigenfunctions.

<sup>\*</sup>Now at OzGrav, School of Physics, University of Melbourne, Parkville, Victoria 3010, Australia.

<sup>†</sup>Now at Department of Earth Sciences, ETH Zürich, 8092 Zürich, Switzerland.

<sup>‡</sup>Now at Department of Earth, Environmental and Planetary Sciences, Brown University, Providence, Rhode Island 02912, U.S.A.

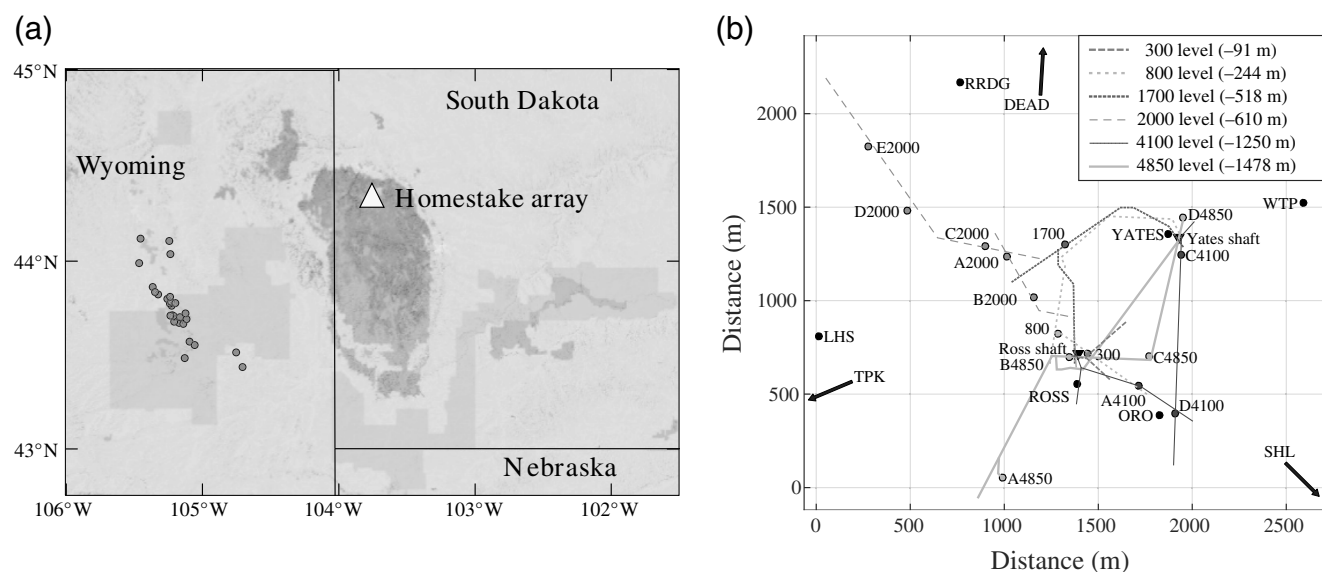


**Figure 1.** (a) The location of the Homestake seismometer array (large triangle) and the estimated origin of the mine blasts used for the analysis (dots). The mine blasts are all estimated as coming from the Powder River Basin in Wyoming. The points on the map in (b) show the sensor locations in and around the Homestake Mine. Lines indicate drifts in which the sensors were placed at varying depths.

In this article, we confirm that observations of surface-wave amplitudes match expectations as a function of depth. These observations are collected from an array of instruments in and around the Sanford Underground Research Facility, previously the Homestake Gold Mine, in South Dakota, United States (Mandic *et al.*, 2018). An array of 24 broadband instruments (15 underground and 9 above ground) was deployed in a 3D array geometry in the otherwise mostly abandoned shafts of the mine, covering a volume roughly 1500 m in depth and 5 km in lateral width. A map similar to the one in Mandic *et al.* (2018) is shown in Figure 1b. Blasts from nearby mines, on average roughly 130 km away, provide a source of seismic excitations used for our observations of surface-wave amplitudes as a function of depth, in the 0.4–1.2 Hz frequency range. These observations are compared with predictions of both Rayleigh- and Love-wave eigenfunctions from two different approaches: (1) by describing the eigenfunctions with a relatively simple biexponential model that would perfectly describe the decay with depth for half-space or power-law velocity models (Haney and Tsai, 2015) and (2) by constraining a 1D velocity profile from ambient-noise cross correlations and then numerically predicting eigenfunctions. As will be shown, the classic formulations of surface-wave eigenfunctions accurately describe the observations.

## Methods

### Observational Methods

The Homestake array is situated in a region of the United States with relatively few local earthquakes, but the Powder River Basin 130 km west of the mine is a very active coal-mining district. The array recorded dozens of signals

created by mining explosions from the Powder River Basin every workday. Typical seismograms created by these explosions were shown by Mandic *et al.* (2018) along with a map of event location estimates for six months of the experiment. The event locations were estimated from a combination of phased array measurements on  $P$  waves combined with  $P$ - and  $S$ -phase time picks made on array stations and a sparse virtual network assembled from open data we obtained from the Incorporated Research Institutions for Seismology data center. Using the Antelope software package, we refined the initial  $P$  and  $S$  picks from “dbdetect” using “dbloc2,” an earthquake location program, and “dbxcor,” a seismogram cross-correlation program. Details on the procedures used to prepare the event catalog used here can be found in Mandic *et al.* (2018).

We used a subset of signals from 28 mining explosions that were recorded in July 2015. The estimated location of these blasts along with the location of the Homestake array are overlaid on a map of the upper midwestern United States in Figure 1a.

For each transient event, we rotate to radial (i.e., longitudinal) and transverse coordinates using the estimate of the blast location. We filter the waveforms to the frequency band from 0.4 to 1.2 Hz because this is where most of the surface-wave power is concentrated for the mine blasts (explained more later) and then calculate Fourier transforms in 10 s segments over a broad time window around the expected surface-wave arrival time. We refer to the radial data point at frequency  $f$  and time  $t$  in seismometer  $i$  located at depth  $z_i$  as  $\tilde{R}_i(f, t; z_i)$  and the corresponding vertical and transverse data points as  $\tilde{V}_i(f, t; z_i)$  and  $\tilde{T}_i(f, t; z_i)$ .

To confirm that Rayleigh waves are dominating our signal on the radial and vertical channels, we identify times

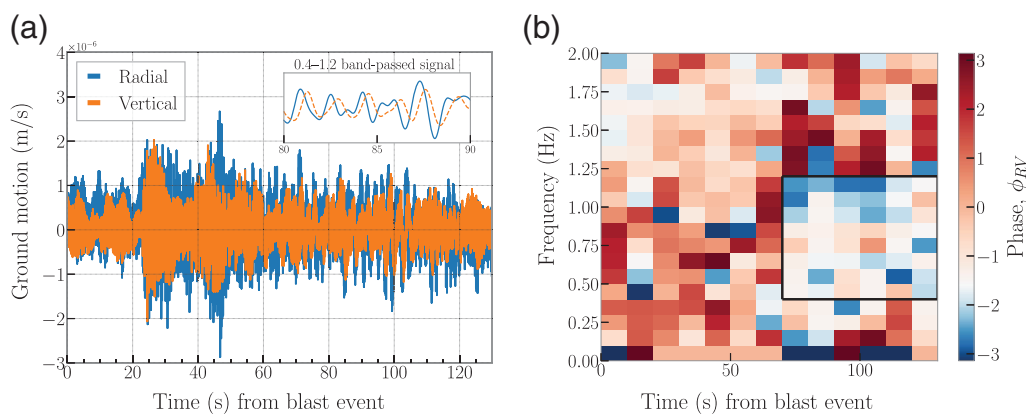


**Figure 2.** (a) Example of analysis applied to surface station seismometer vertical and radial channels for an event on 23 July 2015. (Inset) The signal from 80 to 90 s bandpassed between 0.4 and 1.2 Hz and the vertical trace clearly following the radial trace. (b) The vertical-to-radial phase  $\phi_{RV}$  for the same station over the same time frame. We use 10 s discrete Fourier transforms. The color bar is normalized such that white indicates a phase of  $-\pi/2$ , which corresponds to retrograde motion.

and frequencies when the relative phase between the channels is consistent with retrograde particle motion along the radial direction. This phase is measured by cross correlating the horizontal and vertical channels:

$$\phi_{RV}(f, t; z_i) = \arctan \left[ \frac{\text{Im}(\tilde{R}_i^*(f, t; z_i) \times \tilde{V}_i(f, t; z_i))}{\text{Re}(\tilde{R}_i^*(f, t; z_i) \times \tilde{V}_i(f, t; z_i))} \right]. \quad (1)$$

The asterisk indicates complex conjugation, “Im” indicates the imaginary part of the cross correlation, and “Re” indicates the real part. Figure 2a,b shows the radial and vertical displacements of one example event and the phase as a function of frequency in each 10 s window. Because white regions of this plot indicate the desired phase of  $-\pi/2$ , we observe evidence for retrograde Rayleigh-wave motion between 70 and 130 s and 0.4 and 1.2 Hz. With similar observations for all other events, we restrict further analysis to this frequency range and times when there is clear evidence for vertical and radial motions that are close to being exactly out of phase.

In addition to simply confirming the presence of Rayleigh waves in our data, we restrict our measurements to these periods of retrograde (or later, also prograde) particle motion by projecting the data onto the phasor with the appropriate phase angle:

$$\tilde{\mathcal{R}}_i(f, t; z_i) = -|\tilde{R}_i(f, t; z_i)| \times \text{Im} e^{i\phi_{RV}}. \quad (2)$$

in which vertical lines indicate modulus. The minus sign is used to impose the condition that measurements consistent with retrograde motion are positive, whereas those consistent with prograde motion are negative.  $\tilde{\mathcal{R}}_i(f, t; z_i)$  is now a real-valued quantity. The fact that the radial component will be negative at some depth is consistent with the analytic theory of eigenfunctions, and the difference between prograde and retrograde motions is important to note in regions with a strong velocity contrast (e.g., Tanimoto and Rivera, 2005)

or may be used to distinguish the fundamental mode from higher order modes of propagation (e.g., Boué *et al.*, 2016; Gribler *et al.*, 2016).

Before collecting the amplitudes from all events, we normalize the Rayleigh-wave amplitudes within each event such that the radial component of motion will be  $\sim 1$  at the surface. The average of radial measurements from the nine surface stations for a given time and frequency is used as normalization for all stations’ radial and vertical components. Normalized amplitudes that remain greater than 1.5 are considered outliers and are removed; this removes  $\sim 15\%$  of the individual 10 s observations.

To estimate the Love-wave eigenfunctions, we use data from the same time period as for Rayleigh waves and use a similar procedure for the transverse data: normalize all data points by the mean of the transverse channel on the surface for the corresponding data point and implement a similar restriction on the normalized amplitude of 1.5. It may be expected that Love waves travel at a slightly different velocity from Rayleigh waves, but the difference in arrival time is small compared with the windows of time used. The final observations are shown in the [Results: Observations and Model Estimates](#) section.

#### Eigenfunction Model Parameters for a Simple Model

Our observations indicate a decay with depth that may be consistent with standard models of surface-wave eigenfunctions, and we first test this with a model that is as simple as possible. Boore and Joyner (1997) showed that near-surface geology can often be well approximated with shear-wave velocities that increase as a power-law with depth, and Haney and Tsai (2015) show that a biexponential description of surface-wave eigenfunctions is appropriate for such a model. A similar parameterization can be used for the Rayleigh-wave equations of motion in a half-space, but the fact that it is appropriate for a power-law model as well

allows for a more flexible range of coefficients and eigenfunction shapes.

We use our measurements to estimate the parameters in the following biexponential model for Rayleigh waves' radial and vertical displacements  $m_R$  and  $m_V$  and a single-exponential model for Love waves  $m_L$ . These models depend on a set of intrinsic model parameters  $\theta_R$  and  $a_L$ , the depth  $z$ , and the frequency  $f$  as

$$m_R(f, z; \theta_R) = \left( \exp \left[ -2\pi f z \frac{a_1}{c_R(f)} \right] + A_R \exp \left[ -2\pi f z \frac{a_2}{c_R(f)} \right] \right) \times \frac{1}{1 + A_R} \quad (3)$$

$$m_V(f, z; \theta_R) = \left( \exp \left[ -2\pi f z \frac{a_3}{c_R(f)} \right] + A_V \exp \left[ -2\pi f z \frac{a_4}{c_R(f)} \right] \right) \times \frac{N_{vh}}{1 + A_V} \quad (4)$$

$$m_L(f, z; a_L) = \exp \left[ -2\pi f z \frac{a_L}{c_L(f)} \right]. \quad (5)$$

The full list of parameters to be estimated from observations for Rayleigh waves is  $\theta_R = (N_{vh}, A_R, A_V, a_1, a_2, a_3, a_4)$ , and for Love waves, the single parameter is  $a_L$ . Our observations of  $m_R$ ,  $m_V$ , and  $m_L$  are the amplitudes averaged for all events and all stations at a given depth and frequency. The phase velocities for Rayleigh and Love waves  $c_R(f)$  and  $c_L(f)$  are estimated using ambient-noise correlations, respectively (see the [Eigenfunction Predictions from a Velocity Model](#) section). The assumption that the parameters  $\theta_R$  and  $a_L$  do not change with frequency is intrinsic to the theoretical model outlined by [Haney and Tsai \(2015\)](#) and in principle could be relaxed, but we keep the model here as simple as possible.

We use the `MultiNest` package ([Feroz et al., 2009](#)) to perform a nested sampling analysis to estimate these model parameters. `MultiNest` is commonly used in the astrophysics community, is designed to efficiently sample multimodal distributions and large parameter spaces, and offers robust Bayesian evidence estimates. We discuss further details related to the nested sampling approach in the [Appendix](#) along with more details related to the parameter estimates. The results of this model are shown in the [Results: Observations and Model Estimates](#) section.

#### Eigenfunction Predictions from a Velocity Model

We can also estimate the eigenfunctions for a more arbitrary velocity model, following the ambient-noise cross-correlation methodology that is now relatively commonly used to recover subsurface velocity estimates. We will use this approach as an independent check of the approach presented in the previous section, so we will use velocities estimated

directly from ambient-noise cross correlations rather than from the mine-blast data used earlier. Ambient-noise cross correlations are collected for each station pair using 1 yr of data, from 1 June 2015 to 31 May 2016. Standard methods of time-domain normalization with a 2.56 s running window and spectral whitening for three-component data (i.e., [Bensen et al., 2007](#); [Lin et al., 2008](#)) are used to reduce nonstationary signals in the ambient noise. The cross correlations for a given pair are computed for each component (vertical–vertical, north–north, and east–east) and then the horizontal components are rotated to recover radial and transverse motions used for surface-wave observations.

To develop a 1D model for shear-wave velocities, compression-wave velocities, and density, a starting model is iteratively perturbed until synthetic surface-wave velocity dispersion curves best match observations. Dispersion curves are observed from the noise cross correlations through multiple narrow, Gaussian bandpass filters using the automated FTAN package (as described by [Levshin and Ritzwoller, 2001](#)). Between 0.2 and 7 Hz, Rayleigh and Love group velocities were clearly observed, as were Rayleigh phase velocities, shown in [Figure 3b–d](#) respectively, but the Love phase velocities reported showed very high variability and so were not used in the subsequent analysis. A starting 1D shear-wave velocity model is estimated using the nearest node of the relatively coarse U.S.-wide model of [Schmandt et al. \(2015\)](#) below 3 km depth and the smoothly varying “very-hard rock” profile of [Boore and Joyner \(1997\)](#) above 3 km. The computer package `Computer Programs in Seismology` by [Herrmann \(2013\)](#) is used to invert for a new 1D velocity model, shown in [Figure 3a](#). We use 12 iterations, updating the 1D velocity model to reduce the misfit between observed and predicted dispersion curves (final dispersion curves are shown in [Fig. 3b–d](#)). To understand our final velocity model's resolution with depth and the dependence on the choice of background starting model, 1000 realizations of the starting model are perturbed by an amount drawn from a Gaussian distribution with standard deviation of 10% and the inversion repeated. The gray confidence interval in [Figure 3a](#) shows the 1st and 99th percentiles of these output models, suggesting that even down to 2.5 km, the model is relatively well constrained. Also, there appears to be a low-velocity zone around 1.5 km depth (which is the depth of our deepest stations) that is less well constrained. Nevertheless, we believe this model provides a reasonable estimate of seismic velocities in the region and is sufficiently complex to produce numeric eigenfunctions that may deviate from the simpler biexponential fits described in the previous section.

We finally note that our model is relatively smooth as a function of depth and therefore only approximately fits the observed dispersion data. More sophisticated approaches to solve for 1D velocity structures exist in the literature (e.g., [Bodin et al., 2012](#)), but this is not the focus of this study because further changes to the velocity model will have at most a second-order effect on the actual eigenfunctions predicted ([Haney and Tsai, 2015](#)).

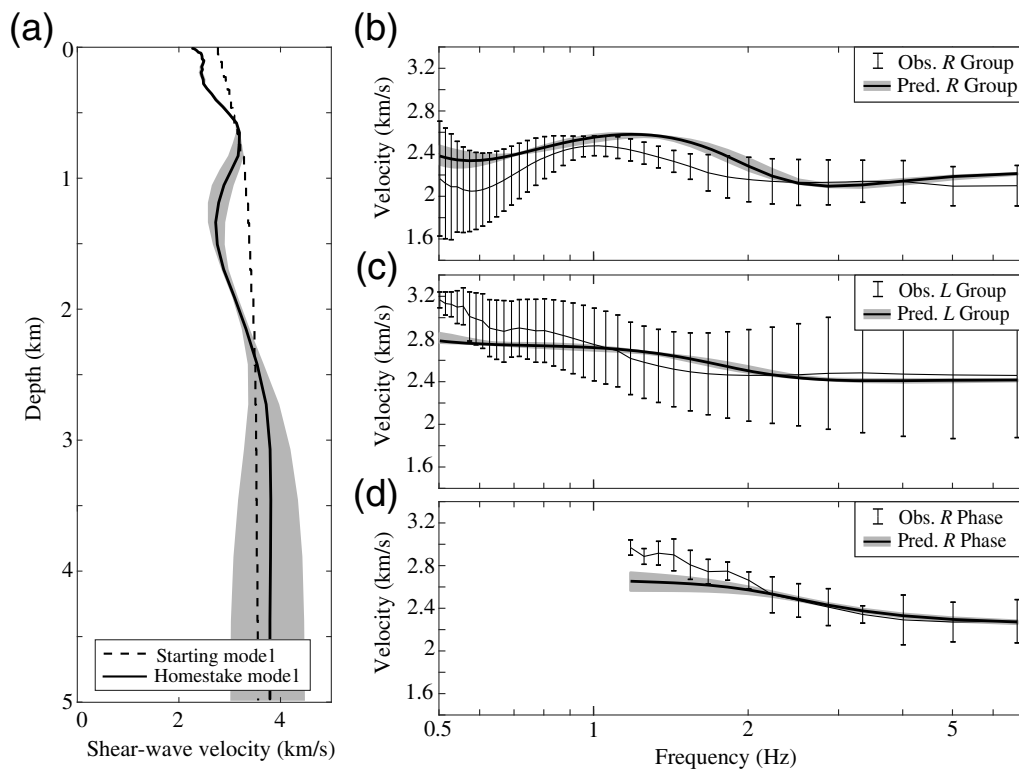


**Figure 3.** (a) The velocity model resulting from ambient-noise travel-time observations and the estimated and measured dispersion curves for (b) *R*-wave group, (c) *L*-wave group, and (d) *R*-wave phase velocities. Gray confidence intervals in all plots represent the 1st and 99th percentiles of models in which the starting model was perturbed by  $\pm 10\%$ .  $1\sigma$  error bars on the observed group, and phase velocities are also shown in (b–d). Obs., observed; Pred., predicted.

### Results: Observations and Model Estimates

An example of the normalized measurements for radial, vertical, and transverse data at 0.9 Hz is shown in Figure 4. Similar plots can also be made for each 0.1 Hz frequency band between 0.4 and 1.2 Hz. Measurements are grouped at distinct depths because stations were deployed at the surface or only at particular levels within the mine. These measurements are qualitatively consistent with what is expected for surface-wave eigenfunctions. The radial component shows an exponential decay in depth and subsequent sign flip, the vertical component shows an initial growth in amplitude followed by a decay at larger depths, and the transverse data points also show an obvious decay with depth.

Figures 5 and 6 show a comparison between the data points estimated from blast events, the simple biexponential model (single exponential for Love waves), and the independent estimate of the surface-wave eigenfunctions made using the velocity model discussed in the [Eigenfunction Predictions from a Velocity Model](#) section. In both figures, we represent the fit of the simple exponential model by drawing randomly from the posterior distribution for the parameters in the model, using these values to construct a realization of the model, and then repeating this several hundred times. We then fill between the 10th and 90th percentiles of those realizations evaluated at each depth. This results

in a very narrow line, as we fit across several frequencies and depths. The lines for the radial and transverse fits are especially narrow at shallow depths because these models are fixed to be one on the surface. The posterior distributions and mean values for the parameters that govern the shape of the biexponential model are presented and discussed in the [Appendix](#).

For Rayleigh waves, the overall shape of the biexponential fits using the nested sampling analysis tracks the data points qualitatively, although there are distinct differences between the depth dependence predicted by the model and the data points in several places. Some of this misfit is likely due to the simplicity of the biexponential model, which fixes the value of the biexponential parameters to be the same for each frequency. Again, one of the fundamental assumptions of this biexponential model is that the velocity increases as a power law with depth (Boore and Joyner, 1997; Haney and Tsai, 2015). Such a power-law velocity model assumption is clearly a simplification, with Homestake's geology being more complex (Noble *et al.*, 1949; Pariseau *et al.*, 1989, 1995, 1996).

The more complex velocity model estimated from the ambient-noise inversion for structure matches the amplitude observations better at some depths and frequencies despite being a completely independent test (i.e., different data, different method—velocity instead of amplitude observations).

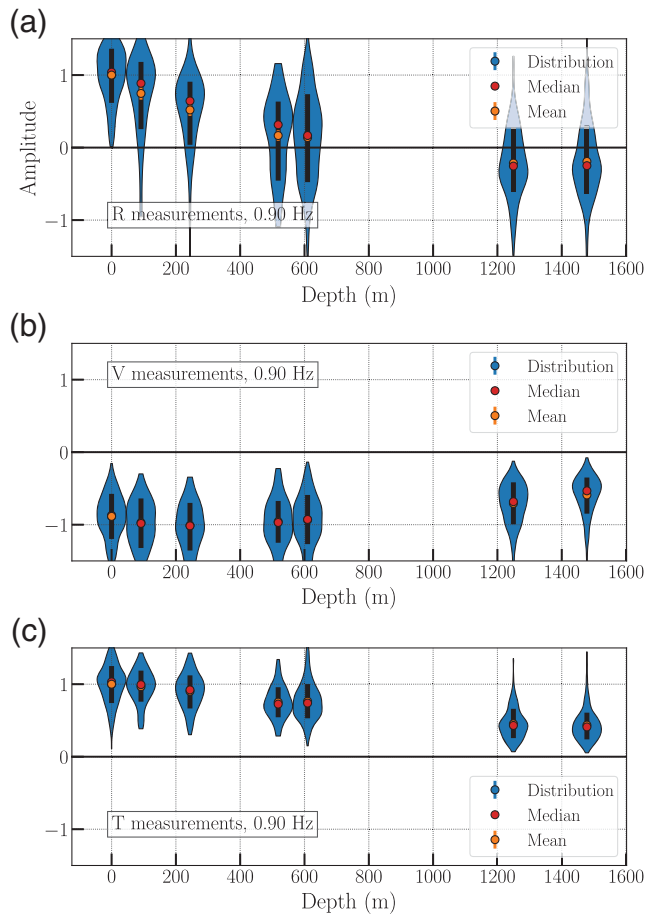


**Figure 4.** (a) The distribution of radial measurements shown by the blue violin plot for measurements at 0.90 Hz. Red and orange points indicate the median and mean of the distribution, respectively, and black bars indicate the 16th and 84th percentiles of the distributions shown in blue. (b,c) The same except for the vertical and transverse measurements.

Comparing the velocity models themselves, the inferred velocity model shown in Figure 3a also shows that a simple power-law model is only sufficient as a first-order approximation. Even this model inferred from ambient noise, however, is also undoubtedly smoother than true geologic discontinuities would warrant and represents a 1D average over the entire region of the array. We also note that some of the deeper observations are fit better by the simple biexponential fit (e.g., at  $\sim 1500$  m in Fig. 5e). In this case, we suspect we suffer from a lack of resolution in the low-velocity zone at this depth, so perhaps the direct eigenfunction observations and fitting is still beneficial. However, both models match the observed mine-blast data reasonably well, suggesting that the theory of Rayleigh waves itself is quantitatively accurate.

In the case of Love waves in Figure 6, both models again fit the data reasonably well. The data show a potentially more variable shape in the shallower measurements and higher frequency estimates than a simple exponential decay. Although the error bars on the individual observations are large enough

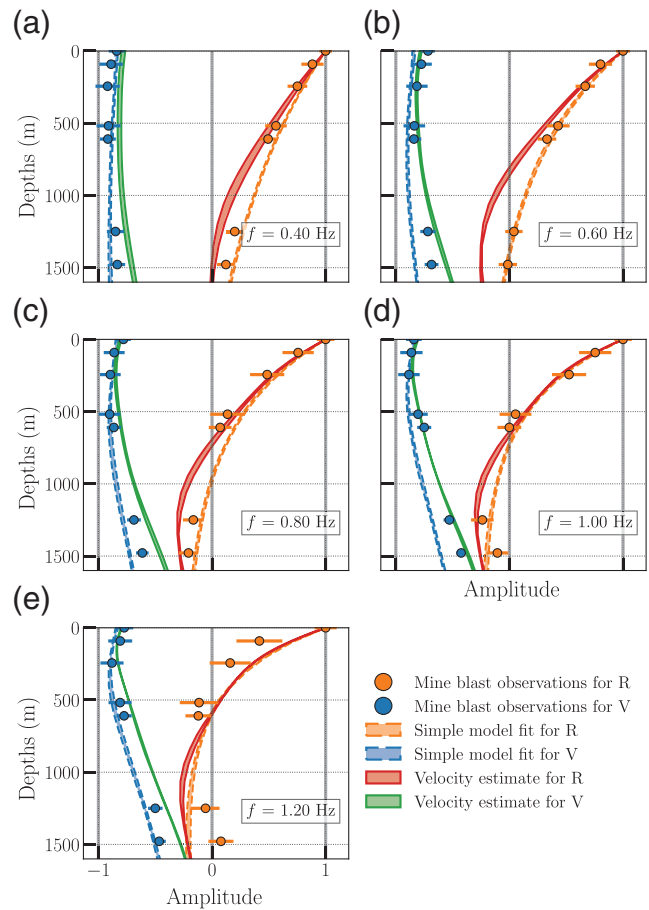


**Figure 5.** (a–e) Rayleigh-wave eigenfunction measurements and estimates at frequencies between 0.4 and 1.2 Hz. In each panel, the scatter plot points are the radial (R) and vertical (V) measurements from the mine blasts. Curves outlined with dashed lines are generated using random draws from the posterior distributions for the parameters of the biexponential models defined in equation (3) to construct realizations of the biexponential model. The widths of those lines represent the 10th and 90th percentiles at each depth of the generated models. Curves outlined in solid lines represent the estimate of the eigenfunctions using ambient-noise correlations and inversion discussed in the [Eigenfunction Predictions from a Velocity Model](#) section. The width of these curves represents the 10th and 90th percentiles for the inversion results from the 1000 random perturbations to the starting model.

to each individually be consistent with an exponential decay, the variability does appear consistent in both the observations and in the numerically generated eigenfunctions that are estimated from the ambient-noise velocity inversion. The exponential fit can describe the overall shape across the full range of frequencies, but the simple single-exponential shape cannot capture any sort of variability in the near surface that might arise in higher frequency measurements (Fig. 6e). For a deeper structure, then, the model-fitting method to be preferred depends on one's confidence in the background starting model or on one's confidence in the power law with depth-dependence assumption in the absence of other information.

The comparison of these two methods to the observational data also serves to highlight the differences in the

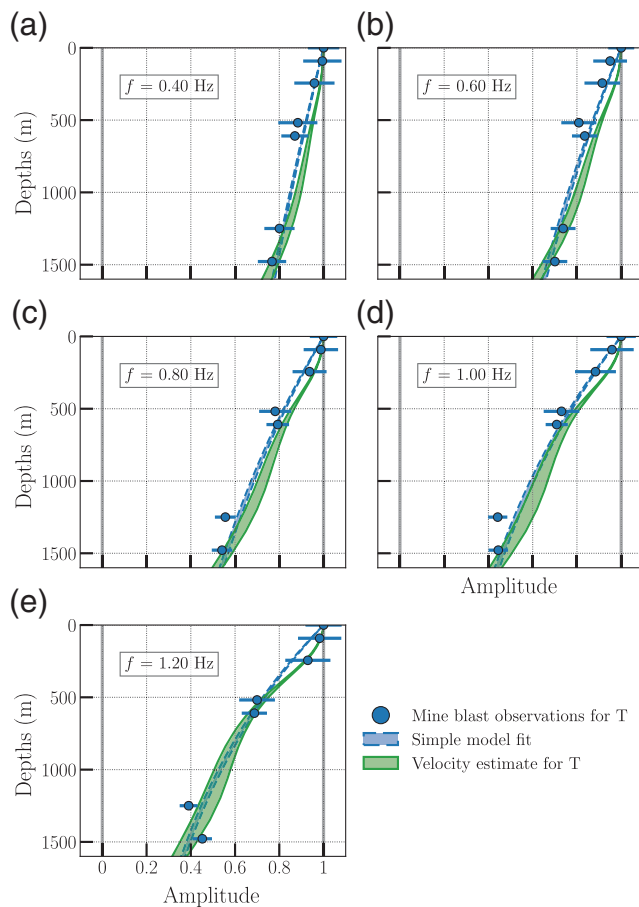


**Figure 6.** (a–e) Love-wave eigenfunction measurements and estimates at frequencies between 0.4 and 1.2 Hz. In each panel, the scatter plot points are the transverse (T) measurements from the mine blasts. Curves outlined with dashed lines are generated using random draws from the posterior distribution for the single exponential model for the Love-wave eigenfunction to construct realizations of that model. The width of those curves represents the 10th and 90th percentiles of the estimated models at each depth. Curves outlined with solid lines are the estimates made using ambient-noise correlations and inversion discussed in the [Eigenfunction Predictions from a Velocity Model](#) section. The widths of these curves represent the 10th and 90th percentiles for the inversion results from the 1000 random perturbations to the starting model.

strengths and weaknesses of the different methods for estimating surface-wave eigenfunctions. It confirms that traditional inversion methods based on ambient-noise correlations are well founded based not just on theoretical grounds but also on direct observational grounds. The comparison with a simple model that assumes a power-law *S*-wave velocity depth profile serves to further highlight the strengths and weaknesses of the inversion method.

### Conclusions

Despite the success of the Earth structure estimation based on seismological surface-wave theory, one of the fundamental predictions of the theory itself—the decay of amplitude of those waves with increasing depth—has not

been directly measured to this point. Using data from mine blasts observed by the Homestake 3D array, we presented direct observational evidence for that decay, along with validation of the predicted flip from retrograde to prograde particle motion for Rayleigh waves at the appropriate depth.

We tested measured decay properties with predictions from two isotropic, radially symmetric Earth models. The first, a simple model based on a power-law shear-wave velocity depth profile, shows qualitatively reasonable results. The second, an inversion technique that used ambient-noise cross correlations to estimate that depth profile, served as an independent verification that the general tenets of surface-wave theory can be used to independently verify the surface-wave eigenfunctions. Extensions of this work could include directly observing the depth dependence of ambient-noise correlations. To directly observe the depth dependence of either the mine blasts or ambient noise, the 3D nature of the Homestake array is vital and thus serves a unique purpose among seismometer arrays.

### Data and Resources

Data presented here were collected at the Homestake 3D seismometer array. The data are available at the Incorporated Research Institutions for Seismology (IRIS) Data Management Center available at [www.iris.edu](http://www.iris.edu) (last accessed July 2018), designation X6. Finding a model to fit dispersion data was done using Computer Programs in Seismology, v.3.30, at <http://www.eas.slu.edu/eqc/eqccps.html> (last accessed March 2016).

### Acknowledgments

The authors are grateful to staff at the Sanford Underground Research Facility and Program for the Array Seismic Studies of the Continental Lithosphere (PASSCAL) for their assistance. Specifically, they thank Jaret Heise, Tom Regan, Bryce Pietzyk, and Jamey Tollefson. Vital technical contributions related to the operation and maintenance of the Homestake 3D seismometer array were made by Terry Stigall. The authors also thank two anonymous reviewers for their helpful comments and suggestions. This work was supported by National Science Foundation (NSF) INSPIRE (Integrated NSF Support Promoting Interdisciplinary Research and Education) Grant PHY1344265. Parts of this research were conducted by the Australian Research Council Centre of Excellence for Gravitational Wave Discovery (OzGrav), through Project Number CE170100004. The authors are grateful for computational resources provided by the Laser Interferometer Gravitational-Wave Observatory (LIGO) Laboratory and supported by National Science Foundation Grants PHY-0757058 and PHY-0823459.

### References

- Aki, K., and P. G. Richards (2002). *Quantitative Seismology*, Second Ed., University Science Books, Sausalito, California.
- Bensen, G. D., M. H. Ritzwoller, M. P. Barmin, A. L. Levshin, F. Lin, M. P. Moschetti, N. M. Shapiro, and Y. Yang (2007). Processing seismic ambient noise data to obtain reliable broad-band surface wave dispersion measurements, *Geophys. J. Int.* **169**, no. 3, 1239–1260.
- Bodin, T., M. Sambridge, H. Tkalčić, P. Arroucau, K. Gallagher, and N. Rawlinson (2012). Transdimensional inversion of receiver functions and surface wave dispersion, *J. Geophys. Res.* **117**, no. B2, doi: [10.1029/2011JB008560](https://doi.org/10.1029/2011JB008560).

- Boore, D. M., and W. B. Joyner (1997). Site amplifications for generic rock sites, *Bull. Seismol. Soc. Am.* **87**, no. 2, 327–341.
- Boúe, P., M. Denolle, N. Hirata, S. Nakagawa, and G. C. Beroza (2016). Beyond basin resonance: Characterizing wave propagation using a dense array and the ambient seismic field, *Geophys. J. Int.* **206**, no. 2, 1261–1272.
- Duputel, Z., L. Rivera, H. Kanamori, and G. Hayes (2012). W phase source inversion for moderate to large earthquakes (1990–2010), *Geophys. J. Int.* **189**, 1125–1147.
- Dziewonski, A. M., and D. L. Anderson (1981). Preliminary reference Earth model, *Phys. Earth Planet. In.* **25**, 297–356.
- Feroz, F., M. P. Hobson, and M. Bridges (2009). MultiNest: An efficient and robust Bayesian inference tool for cosmology and particle physics, *Mon. Not. Roy. Astron. Soc.* **398**, no. 4, 1601–1614.
- Gribler, G., L. M. Liberty, T. D. Mikesell, and P. Michaels (2016). Isolating retrograde and prograde Rayleigh-wave modes using a polarity mute, *Geophysics* **81**, no. 5, V379–V385.
- Haney, M. M., and V. C. Tsai (2015). Nonperturbational surface-wave inversion: A Dix-type relation for surface waves, *Geophysics* **80**, no. 6, EN167–EN177.
- Herrmann, R. B. (2013). Computer programs in seismology: An evolving tool for instruction and research, *Seismol. Res. Lett.* **84**, no. 6, 1081–1088.
- Kawase, H., and K. Aki (1989). A study on the response of a soft basin for incident S, P, and Rayleigh waves with special reference to the long duration observed in Mexico City, *Bull. Seismol. Soc. Am.* **79**, no. 5, 1361–1382.
- Levshin, A. L., and M. H. Ritzwoller (2001). Automated detection, extraction, and measurement of regional surface waves, *Pure Appl. Geophys.*, **158**, no. 8, 1531–1545, doi: [10.1007/PL00001233](https://doi.org/10.1007/PL00001233).
- Li, Y. G., and P. C. Leary (1990). Fault zone trapped seismic waves, *Bull. Seismol. Soc. Am.* **80**, no. 5, 1245–1271.
- Lin, F.-C., M. P. Moschetti, and M. H. Ritzwoller (2008). Surface wave tomography of the western United States from ambient seismic noise: Rayleigh and Love wave phase velocity maps, *Geophys. J. Int.* **173**, no. 1, 281–298.
- Mandic, V., V. C. Tsai, G. L. Pavlis, T. Prestegard, D. C. Bowden, P. Meyers, and R. Caton (2018). A 3D broadband seismometer array experiment at the Homestake Mine, *Seismol. Res. Lett.* **89**, no. 6, 2420–2429.
- Nakamura, Y. (1989). A method for dynamic characteristics estimation of subsurface using microtremor on the ground surface, *Q. Rep. Railway Tech. Res. Inst.* **30**, no. 1, 25–33.
- Noble, J. A., J. O. Harder, and A. L. Slaughter (1949). Structure of a part of the northern Black Hills and the Homestake Mine, Lead, South Dakota, *Geol. Soc. Am. Bull.* **60**, no. 2, 321.
- Pariseau, W. G., J. C. Johnson, M. M. McDonald, and M. E. Poad (1995). Rock mechanics study of shaft stability and pillar mining, Homestake Mine, Lead, SD (in three parts): 1, *Premining Geomechanical Modeling Using UTAH2*, Report of Investigations 9618.
- Pariseau, W. G., J. C. Johnson, M. M. McDonald, and M. E. Poad (1996). Rock mechanics study of shaft stability and pillar mining, Homestake Mine, Lead, S.D. (in three parts): 3, *Geomechanical Monitoring and Modeling Using UTAH3*, Report of Investigations 9618.
- Pariseau, W. G., M. Poad, and E. L. Corp (1989). Extended three dimensional finite element analyses of the Homestake Mine study stope, *Proc. International Symposium on Rock at Great Depth*, Pau, France, 28–31 August 1989.
- Peterson, J. R. (1993). Observations and modeling of seismic background noise, *U.S. Geol. Surv. Open File Rept.* 93-322, doi: [10.3133/ofr93322](https://doi.org/10.3133/ofr93322).
- Rayleigh, L. (1885). On waves propagated along the plane surface of an elastic solid, *Proc. Lond. Math. Soc.* **17**, 4–11.
- Schmandt, B., F. C. Lin, and K. E. Karlstrom (2015). Distinct crustal isostasy trends east and west of the Rocky Mountain Front, *Geophys. Res. Lett.* **42**, no. 23, 10,290–10,298.
- Shapiro, N. M., M. Campillo, L. Stehly, and M. H. Ritzwoller (2005). High-resolution surface-wave tomography from ambient seismic noise, *Science* **307**, no. 5715, 1615–1618.
- Takeuchi, H., and M. Saito (1972). Seismic surface waves, in *Seismology: Surface Waves and Earth Oscillations*, B. A. Bolt (Editor), Academic Press, New York, New York, 217–295.
- Tanimoto, T., and L. Rivera (2005). Prograde Rayleigh wave particle motion, *Geophys. J. Int.* **162**, no. 2, 399–405.

## Appendix

### Parameter Estimation Methods

We use our amplitude and phase measurements from mine blasts to estimate the parameters of a biexponential model for the Rayleigh-wave eigenfunctions and an exponential model for the Love-wave eigenfunction. We use  $m_R$  and  $m_V$  to refer to the biexponential models for the Rayleigh-wave radial and vertical eigenfunctions and  $m_L$  for Love waves. These models depend on a set of intrinsic model parameters  $\theta_R$  and  $a_L$ , the depth  $z$ , and the frequency  $f$ . These parameters are related by equation (3) that is the forward model we use for the inversion.

We use the mine-blast data to estimate the best-fit parameters in the biexponential model  $\theta_R = (N_{vh}, A_R, A_V, a_1, a_2, a_3, a_4)$  and  $a_L$  for the single exponential Love-wave model.

We use the MultiNest package, detailed in Feroz *et al.* (2009), to perform the parameter estimation for  $\theta_R$ . MultiNest is commonly used in the astrophysics community and is designed to efficiently sample multimodal distributions and large parameter spaces. It also offers robust Bayesian evidence estimates, which we do not use here. The posterior probability distribution is given by Bayes' theorem

$$p(\theta|\{\bar{r}, \bar{v}\}) = \frac{p(\{\bar{r}, \bar{v}\}|\theta)p(\theta)}{\int d\theta p(\{\bar{r}, \bar{v}\}|\theta)p(\theta)}, \quad (A1)$$

in which  $\bar{r}$  and  $\bar{v}$  are the average normalized displacements over all measurements at a given depth and frequency. They are shown, for example, as the orange points in Figure 4. The likelihood function for the Rayleigh-wave eigenfunctions  $p(\{\bar{r}, \bar{v}\}|\theta_R)$  is taken to be a Gaussian

$$\begin{aligned} \ln p(\{\bar{r}, \bar{v}\}|\theta) \\ = -\frac{1}{2} \sum_f \sum_z \left( \frac{[\bar{r}(f, z) - m_R(f, z; \theta)]^2}{\sigma_r^2(f, z)} + \frac{[\bar{v}(f, z) - m_V(f, z; \theta)]^2}{\sigma_v^2(f, z)} \right). \end{aligned} \quad (A2)$$

We assume that the prior probability distribution  $p(\theta_R)$  can be split into the product of independent Gaussian prior probability distributions on each individual parameter. We use estimates of these parameters from Haney and Tsai (2015) to inform the Gaussian prior probability distributions. The definition of our parameters differs slightly from those in Haney and Tsai (2015), but we can generate prior information on each parameter in our model using a combination of

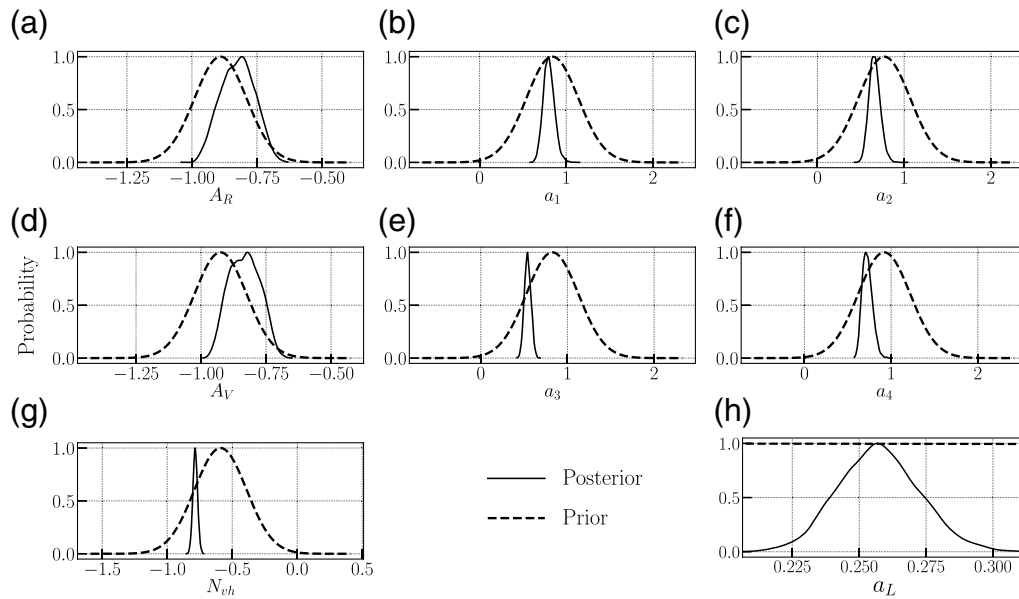


**Figure A1.** Prior (dashed) and posterior (solid) distributions for each parameter in (a–g) the simple Rayleigh-wave biexponential model and (h) the Love-wave exponential model. The parameter associated with each distribution is indicated below each panel.

parameters defined in that paper. We then widen the uncertainty on those parameters significantly to allow for sufficient exploration of the parameter space, given that our situation is likely different from the theoretical one considered in that paper.

The results for the estimates of each parameter are summarized in Table A1, and Figure A1 shows the prior and posterior distributions on each individual parameter.

**Table A1**

Parameter Estimation Results and Prior Information for *R*-Wave and *L*-Wave Eigenfunction Parameters

Parameter	Mean	Standard Deviation	Prior Mean	Prior Standard Deviation
$A_R$	-0.83	0.06	-0.89	0.1
$a_1$	0.80	0.06	0.84	0.1
$a_2$	0.66	0.06	0.77	0.1
$A_V$	-0.83	0.07	-0.92	0.1
$a_3$	0.54	0.04	0.83	0.3
$a_4$	0.73	0.05	0.92	0.3
$N_{vh}$	-0.78	0.02	-0.59	0.2
$a_L^*$	0.26	0.02	0	3

\*This parameter is used in the Love-wave model.

**Patrick Meyers**  
**Tanner Prestegard**  
**Vuk Mandic**

School of Physics and Astronomy  
University of Minnesota  
116 Church Street SE  
Minneapolis, Minnesota 55455 U.S.A.  
pat.meyers@unimelb.edu.au

**Daniel C. Bowden**  
**Victor C. Tsai**

Seismological Laboratory  
California Institute of Technology  
1200 E. California Boulevard, MS 252-21  
Pasadena, California 91125 U.S.A.

**Gary Pavlis**  
**Ross Caton**

Department of Geological Sciences  
Indiana University  
1001 E. 10th Street  
Bloomington, Indiana 47405 U.S.A.

Manuscript received 7 February 2019;  
Published Online 25 June 2019